Bioinspired Integrated Auxetic Elastomers Constructed by a Dual Dynamic Interfacial Healing Strategy

Zhiran Zheng, Jiawei Li, Kailun Wei, Ning Tang, Min-Hui Li, Jun Hu

Bio-inspired Integrated Auxetic Elastomers Constructed by Dual Dynamic Interfacial Healing Strategy

Zhiran Zheng, Jiawei Li, Kailun Wei, Ning Tang, Min-Hui Li, and Jun Hu**

Z. Zheng, J. Li, K. Wei, N. Tang, J. Hu
Beijing Advanced Innovation Center for Soft Matter Science and Engineering, Beijing University of Chemical Technology, North Third Ring Road 15, Chaoyang District, Beijing 100029, China
E-mail: jhu@mail.buct.edu.cn

M.-H. Li
Chimie ParisTech, PSL University, CNRS, Institut de Recherche de Chimie Paris, 11 rue Pierre et Marie Curie, Paris 75005, France
E-mail: min-hui.li@chimieparistech.psl.eu

Keywords: auxetic elastomer, negative Poisson's ratio, dynamic healing, disulfide bonds, hydrogen bonds

Auxetic materials are appealing due to their unique characteristics of transverse expansion while being axially stretched. Nevertheless, current auxetic materials are often produced by the introduction of diverse geometric structures through cutting or other pore-making processes, which heavily weaken their mechanical performance. Inspired by the skeleton-matrix structures in natural organisms, here we report an integrated auxetic elastomer (IAE) composed of high-modulus crosslinked poly(urethane-urea) as a skeleton and low-modulus non-crosslinked poly(urethane-urea) as a complementary-shape matrix. Benefiting from disulfide bonds and hydrogen bonds-promoted dual dynamic interfacial healing, the resulting IAE is flat, void-free, and has no sharp soft-to-hard interface. Its fracture strength and elongation at the break are increased to 400% and 150%, respectively, of the values of corrugated re-entrant skeleton alone, while the negative Poisson's ratio (NPR) reserves within a strain range of 0-104%. In addition, the advantageous mechanical and auxetic properties of this elastomer are further confirmed by finite element analysis. The concept of combining two dissimilar polymers into an integrated hybrid material solves the problem of the deterioration in mechanical performance of auxetic

materials after subtractive manufacturing, while preserves the NPR effect in a large deformation, which provides a promising approach to robust auxetic materials for engineering applications.

1. Introduction

Auxetic materials with negative Poisson's ratio (NPR) show unique characteristics of transverse expansion while being axially stretched,[1] and their performance is generally regulated by diverse geometric structural units rather than chemical compositions.[2,3] This intrinsic feature makes auxetic materials break through the cognitive limitation in mechanical properties of conventional materials, thus being of great significance for basic research,[4,5] engineering applications,[6,7] and people's daily life.[8,9] In recent years, benefiting from the rapid development of advanced additive manufacturing technology and material reduction technology, the research of auxetic materials has made outstanding achievements and realized many counterintuitive performances that are rare or even non-existent in nature.[10-14] For example, Koohbor et al. reported auxetic elastomers with multi-scale NPR structures by introducing orthogonal holes into the planar thermoplastic polyurethane, which exhibited tailorable mechanical properties with spatial adjustment of perforations in the structure.[6] Sun et al. combined chiral structures with shape memory polymers to get auxetic elastomers with specific memory performance.[13] However, the mechanical performance of these auxetic materials including fracture strength and elongation at break are seriously deteriorated, once they go through cutting or other pore-making processes to introduce geometric structures for the achievement of NPR effect. To solve this issue, efforts have been made to explore strong and tough elastomers with two strategies. The first strategy focuses on the formation of additional dynamic forces, such as hydrogen bonding,[15,16] metal-ligand coordination,[17,18] and ionic interactions,[19] to reinforce elastomers. The second strategy incorporates functional additives like nanostructured carbon,[20,21] metals,[22] and low-melting-point alloys[23] into elastomer matrices to improve mechanical performance. Nevertheless, the materials with the first strategy often suffer from low bond energy of reversible associations and cannot get sufficient enhancement in mechanical properties as demanded.[24] On the other hand, the independent components within the materials with the second strategy always bring about inevitable interfacial problems.[25,26] Therefore, the development of alternative approaches to endow elastomers with both robust mechanical properties and the NPR effect is a current hot topic.

Nature is simple and efficient. Many organisms are hybrid materials created by multiscale skeleton-matrix structures from hard and soft ingredients with complementary characteristics,

showing attractive mechanical and functional features that are not accessible by their separate components alone.[27-29] For instance, stiff biological tissues such as nacre, bone, and sea sponge exoskeletons are consisted of multiple hierarchical structures with alternative hard skeleton and soft matrix from nanoscale to macroscale.[30,31] These structures make the materials much tougher than their main hard skeletons alone, yet without sacrificing strength and elongation.[32] Coincidentally, soft tissues including muscle, skin, and tendon display similar skeleton-matrix structures by implanting hard collagen into a soft matrix across multiple spatial scales.[33] In these hybrid materials, the hard ingredients provide strong mechanical strength to against deformation, and the soft components offer good toughness to resist fracture.[34] The variation in stiffness between alternative hard and soft structures is able to produce obstacles on interfaces, which in turn hinder crack propagation by the deflection of cracks. More importantly, these biological tissues are self-healable and their regenerative cells provide sufficient intercellular forces to improve the binding between the hard and soft components and to prolong their service life.[35] It can be seen that self-healing is a kind of "zoetic" approach to constructing skeleton-matrix auxetic materials with enhanced mechanical properties.

Inspired by nature, herein we employ the above skeleton-matrix structure design with auxetic corrugated geometry in the skeleton to develop an integrated corrugated re-entrant elastomer with the NPR effect. As depicted in Scheme 1a, the chemically crosslinked poly(urethane-urea) (PTHF-4AD-DAHP) and the non-crosslinked poly(urethane-urea) (PTHF-4AD) are prepared and used respectively as the hard skeleton and the soft matrix. In both crosslinked PTHF-4AD-DAHP and non-crosslinked PTHF-4AD, the urea and urethane moieties provide abundant donors and receptors to form multiple hydrogen bonds, that can ensure their elastic recovery, toughness, and high fracture energy.[36,37] At the same time, disulfide bonds make the dynamic bond exchange possible,[38,39] endowing them with autonomous healing capacities.[40,41] After cutting PTHF-4AD-DAHP into a corrugated re-entrant structure as a hard skeleton followed by the complementary shape-filling of PTHF-4AD as a soft matrix, an integrated auxetic elastomer (IAE) has been successfully obtained where the dual dynamic interfacial healing is achieved by hydrogen bonds and disulfide bonds (Scheme 1b). The resulting IAE was a flat, void-free, and continuous solid at the macroscopic level, and exhibited a tensile force of 92 N and the Poisson's ratio ranging from −0.13 to 0 in the process of stretching to 104%, which was further confirmed by finite element analysis (FEA). The simultaneous achievement of high mechanical strength, good defect tolerance, and unprecedented auxeticity was promoted by three major factors: 1) the low-modulus matrix offered good ductility to withstand the large deformation for stress dissipation, while the high-modulus skeleton together with the low-modulus matrix

improved mechanical strength; 2) there were no interface problems between the skeleton and the matrix because of the dynamic integration of multiple hydrogen bonds and disulfide bonds; and 3) the rotation, bending, and stretching of the skeleton combined with the ductility of the matrix endowed the IAE with adjustable NPR effect. This work solves the difficulties to fabricate comprehensive auxetic elastomers with robust mechanical properties and the NPR effect. The elaboration process of complementary shape-filling and dual dynamic interfacial healing paves a way for automatic scaled-up synthesis of modular heterogeneous materials, which can be engineered into advanced functional products for applications in metamaterials.

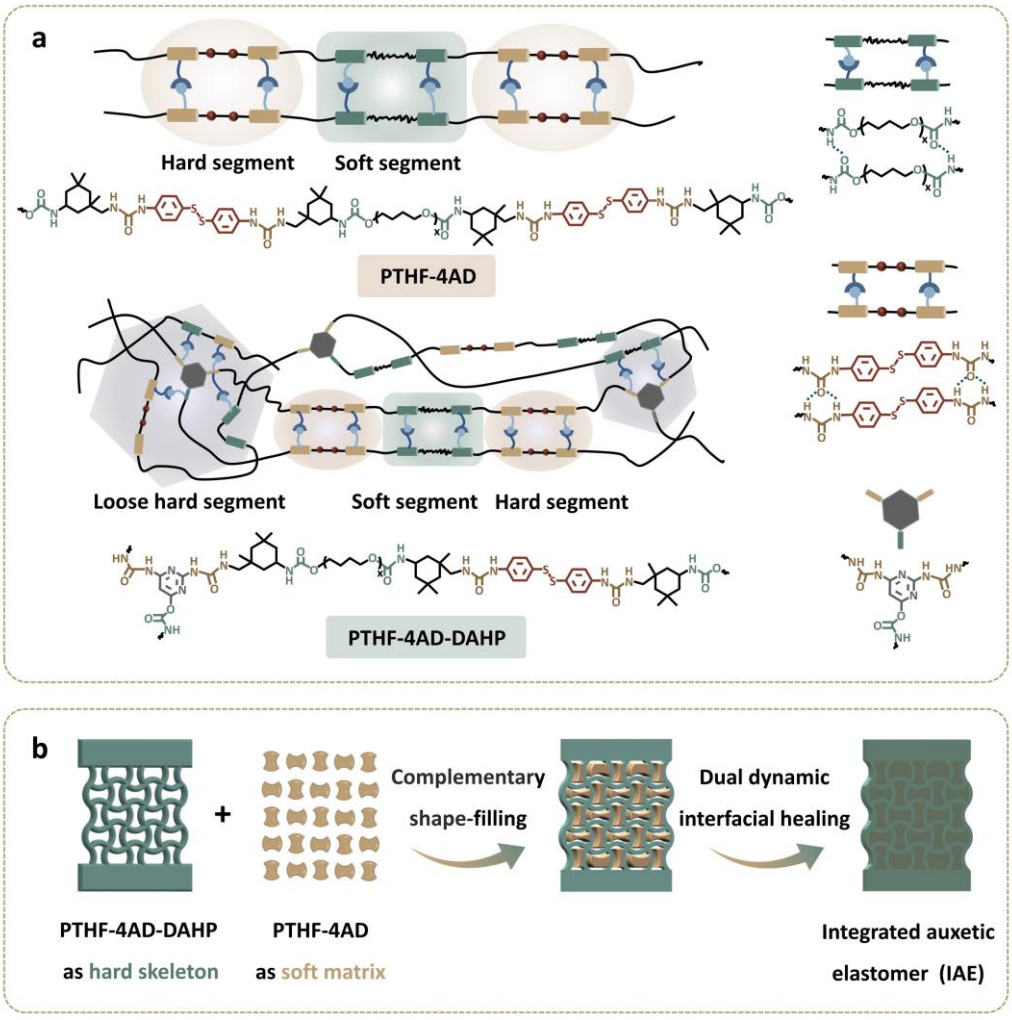

Scheme 1. Elaboration of the integrated auxetic elastomer (IAE). a) Chemical structures of the non-crosslinked PTHF-4AD and the crosslinked PTHF-4AD-DAHP. b) Schematic illustration of the preparation of IAE by using the corrugated re-entrant PTHF-4AD-DAHP as the hard skeleton followed by the complementary shape-filling of PTHF-4AD as the soft matrix through dual dynamic interfacial healing.

2. Results and Discussion

2.1. Structure characterization of PTHF-4AD and PTHF-4AD-DAHP

As illustrated in **Scheme 1**a and S1, the PTHF-4AD was synthesized by a two-step reaction from hydroxyl-terminated polytetrahydrofuran (PTHF), isophorone diisocyanate (IPDI), and a bifunctional chain extender 4-aminophenyl disulfide (4-AD), while the PTHF-4AD-DAHP was polymerized from PTHF, IPDI, 4AD, and trifunctional chain extender 2,4-diamino-6-hydroxy pyrimidine (DAHP). Accordingly, a hard segment in 4-AD-enriched region and a soft segment in PTHF region were generated in PTHF-4AD. On the contrary, in PTHF-4AD-DAHP a hard segment in 4AD-enriched region, a loose hard segment near DAHP domain, and a soft segment in PTHF region were formed. **Figure 1**a showed the transmittance and brownish-yellow colors for PTHF-4AD and PTHF-4AD-DAHP elastomers due to the existence of aromatic groups in 4-AD. The average transmission of PTHF-4AD-DAHP is over 90% in the visible range from 570 to 900 nm, higher than that of PTHF-4AD, because of the relatively low content of 4-AD in PTHF-4AD-DAHP. Size exclusion chromatography (SEC) revealed that the molecular weight (M_w) of PTHF-4AD was 80 kDa with a polydispersity index (PDI) of 1.95 (Figure S1, Supporting Information). Gel content experiments indicated that PTHF-4AD-DAHP owned high gel contents (> 90%) in common solvents (Figure S2, Supporting Information), proving the crosslinked network structure of PTHF-4AD-DAHP. Attenuated total reflection Fourier transform infrared spectra (ATR-FTIR) showed the absence of the characteristic peak of -NCO in both PTHF-4AD and PTHF-4AD-DAHP, but the appearance of the stretching vibration of carbonyl groups of urethane and urea moieties at 1700 and 1650 cm^{-1} (Figure 1b). Moreover, the in-plane bending and stretching vibrations of N-H of urethane and urea units were observed at 1536 and 3340 cm^{-1}, respectively. All above results proved the complete polymerization in both PTHF-4AD and PTHF-4AD-DAHP.

The thermal stability of both samples was studied by thermogravimetric analysis (TGA) (Figure S3, Supporting Information). The initial thermal degradation temperature ($T_{5\%}$) was 284°C and 295°C for PTHF-4AD and PTHF-4AD-DAHP, respectively, showing their good thermal stability. Besides, they exhibited two stages of weight loss, one at 300°C and another at > 400°C. The first stage of the thermal decomposition occurred at 300°C with 10.5% and 14.4% weight loss because of the lower bond energy of disulfide bonds. The second weight loss stage mainly involved the thermal degradation of fatty chains and aromatic rings in networks. X-ray diffractions (XRD) was also performed and showed amorphous structure in both samples (Figure 1c). The broad bump around 2θ ~20° corresponded to an average lateral distance of 0.44 nm between polymer backbones. The absence of crystalline structure was also confirmed by differential scanning calorimetry (DSC) (Figure S4, Supporting Information), where non-

crystalline exothermic peak was observed. 1D, 2D small-angle X-ray scattering (SAXS) and atomic force microscopy (AFM) images revealed the microphase separation in PTHF-4AD, while no significant microphase separation structure was observed for PTHF-4AD-DAHP (inset in Figure 1d and 1e; Figure S5 and S6, Supporting Information). This could be explained by the restriction of chain mobility imposed by the crosslinked structure in PTHF-4AD-DAHP. Dynamic mechanical analysis (DMA) demonstrated that the storage modulus decreased with the temperature increase for both elastomers (Figure S7, Supporting Information). According to Flory's rubber elasticity theory, the crosslinking density (ν_e) of PTHF-4AD-DAHP networks was calculated to be 624.96 mol m^{-3}.[42,43] The ratio of storage modulus over loss modulus changed with the temperature and showed the occurrence of glass transition (T_g). Figure 1d and 1e showed the soft phase T_g (T_{gs}) in PTHF-4AD and PTHF-4AD-DAHP of −42 and −30°C, respectively, and their hard phase T_g (T_{gh}) of −5 and 20°C. The relatively low T_{gs} and T_{gh} could facilitate activation of disulfide bonds in hard segment phase and the healing efficiency of PTHF-4AD and PTHF-4AD-DAHP. To quantify the hydrogen bonding in PTHF-4AD and PTHF-4AD-DAHP, the peak fitting method was employed for signals in the region from 1620 to 1740 cm^{-1} of ATR-FTIR spectra, which belonged to the stretching vibration region of C = O.[44,45] For PTHF-4AD, the disordered hydrogen bonds accounted for 7% (Figure 1f; Table S1, Supporting Information), but it was up to 22% for PTHF-4AD-DAHP (Figure 1g; Table S2, Supporting Information). The increase of the disordered hydrogen bonds was attributed to the steric effect of DAHP that produced loose hard segments in PTHF-4AD-DAHP. Note that the total content of hydrogen bonds for both PTHF-4AD and PTHF-4AD-DAHP was over 50%. Upon heating from 30 to 140°C, the peak intensity representing N-H stretching vibration at 3349 cm^{-1} for PTHF-4AD and 3339 cm^{-1} for PTHF-4D-DAHP decreased partially, which demonstrated the fracture of H-bonded N-H while keeping free N-H unchanged (Figure 1h and 1i). In brief, PTHF-4AD and PTHF-4AD-DAHP had high density of hydrogen bonds yet different molecular chain conformations. Therefore, they exibited distinct mechanical performance as will be discussed in the following section.

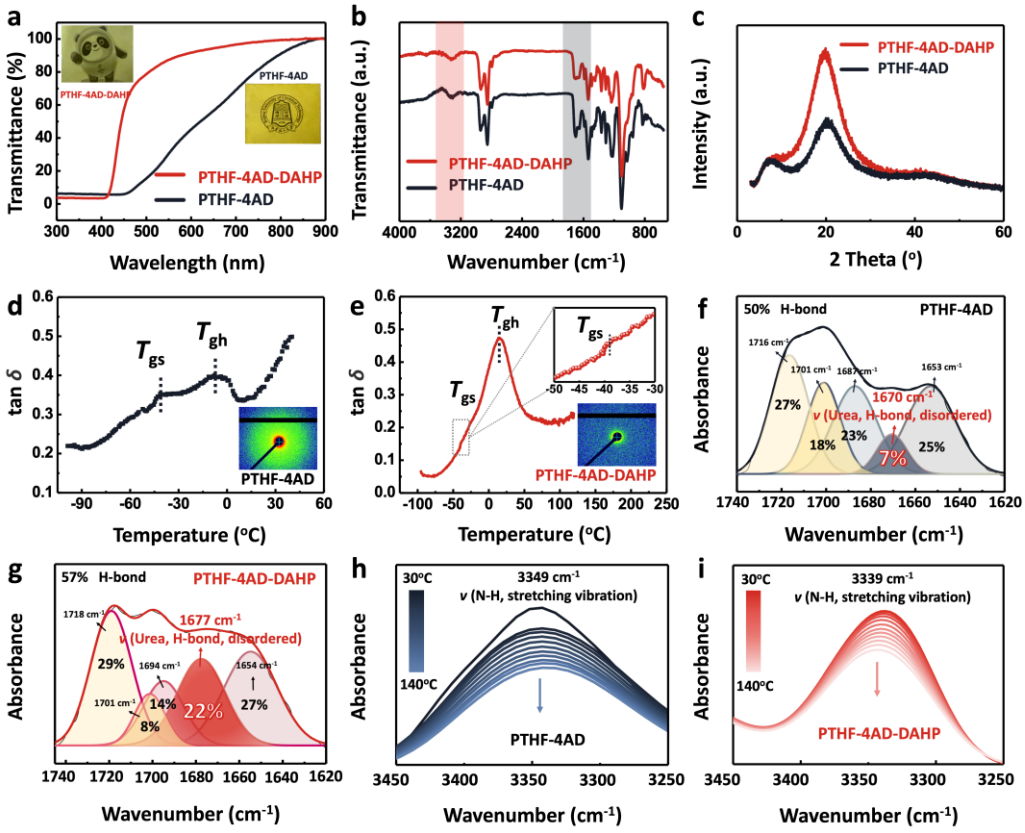

Figure 1. Structure characterization of PTHF-4AD and PTHF-4AD-DAHP. a) Transmission spectra in the range from 300 to 900 nm. Insets: optical photographs of PTHF-4AD and PTHF-4AD-DAHP films on the top of BUCT logo (film thickness = 1 mm). b) ATR-FTIR spectra in the range from 500 to 4000 cm^{-1}. c) XRD patterns in 2θ range from 10 to 60^o with a scan rate of 10^o min^{-1}. Tan δ of d) PTHF-4AD and e) PTHF-4AD-DAHP as a function of temperature. Insets: 2D SAXS (from 0.01-0.24 $Å^{-1}$ of $q = 4\pi \sin(\theta)/\lambda$) image of PTHF-4AD and (from 0.01-0.21 $Å^{-1}$ of q) image of PTHF-4AD-DAHP films. ATR-FTIR spectra and their fitting curves of f) PTHF-4AD and g) PTHF-4AD-DAHP in the region from 1620 to 1740 cm^{-1}. The heavy-color parts were the fitting peaks of the disordered hydrogen bonds. Temperature-dependent ATR-FTIR spectra of h) PTHF-4AD and i) PTHF-4AD-DAHP in the range of 3250-3450 cm^{-1} upon temperature increasing from 30 to 140^{o}C.

2.2. Mechanical and self-healing properties of PTHF-4AD and PTHF-4AD-DAHP

The mechanical behaviors of PTHF-4AD and PTHF-4AD-DAHP were comparatively investigated by using an electronic tensile machine at a stretching rate of 100 mm min^{-1}. PTHF-4AD-DAHP was highly stretchable with a maximum elongation of 778%, the fracture strength of 15.2 MPa, and Young's modulus of 9.4 MPa, which are all higher than those of PTHF-4AD

(714%, 1.6 MPa, and 1.7 MPa) (**Figure 2**a; Figure S8, Supporting Information). The significant differences in the fracture strength and Young's modulus mainly came from the fact that PTHF-4AD-DAHP was chemically crosslinked, but PTHF-4AD were not. Along with the robust mechanical behavior, PTHF-4AD-DAHP owned high fracture energy of 71.3 kJ m^{-2} (Figure 2b), high enough to lift a load ≈1,0000 times heavier than elastomer itself (Figure S9a, Supporting Information). To draw a relationship between stress distribution and fracture, the FEA was employed to illustrate the mode of fracture notch, that is, the stress concentrated at the crack and extended from it. Under this assumption, the higher the fracture energy, the weaker the stress diffusion. Therefore, the high fracture energy of PTHF-4AD-DAHP provided an obstacle to crack propagation (Figure S9b, Supporting Information), making it a high-quality candidate as a strong and tough skeleton.

To investigate the self-healable capacity of PTHF-4AD and PTHF-4AD-DAHP, the rheological measurements were first performed in alternate step strain mode with fixing the frequency of 10 rad s^{-1} at 25ºC. For PTHF-4AD, *G*' showed a higher value than *G*'' at 1% strain, but drastically decreased below *G*'' when a 100% strain was applied. After the removal of high strain and the utilization of a low strain of 1% again, the modulus was recovered with a certain reduction (Figure 2c). These observations strongly demonstrated the good self-healable capacity of PTHF-4AD. Similarly, the PTHF-4AD-DAHP displayed a quick recovery of *G*' and *G*'' under the alternate large and small strains (Figure 2d), despite its chemical crosslinking structure. The self-healing efficiency of samples at macroscopic level was further evaluated by using tensile tests. After self-healing at 25ºC for 7 h, the self-healed PTHF-4AD exhibited similar strength (1.6 MPa) and stretchability (695%) to those of the virgin sample (Figure 1e; Table S3, Supporting Information). On the other hand, the fracture strength and elongation at break of PTHF-4AD-DAHP were 14.8 MPa and 768% after self-healing at 25ºC for 24 h, with a recovery efficiency of 98% (Figure 2f; Table S3, Supporting Information). Besides the satisfactory self-healing properties, PTHF-4AD and PTHF-4AD-DAHP were also recyclable (Figure S10, Supporting Information). The fracture strength and elongation at break of the recycled PTHF-4AD and PTHF-4AD-DAHP were 1.1 MPa, 798%, and 14.8 MPa, 804%, respectively, with the recycling efficiency over 80%.

During above "network reconstruction" processes, disulfide bonds and hydrogen bonds inside PTHF-4AD and PTHF-4AD-DAHP were considered to play a key role. The stretching vibration peak at 472 cm^{-1} in Raman spectra should be assigned to disulfide bonds (Figure 2g). [46] As a kind of relative weak covalent bond, the exchange of disulfide bonds normally requires less energy. Once S-S bonds were replaced with C-C bonds as illustrated in the control

elastomers, namely PTHF-4ED and PTHF-4ED-DAHP, their self-healing efficiency declined dramatically to only 74% and 59% (Figure S11; Table S4, Supporting Information), demonstrating that disulfide bonds were crucial in this self-healing process, and the partial reserved self-healing effect was attributed to the presence of hydrogen bonds. The self-adhesive capacity of PTHF-4AD-DAHP was studied by AFM, as the free urethane and urea groups can form hydrogen bonds with hydroxyl groups at the tip of AFM probe (Figure S12, Supporting Information). The average adhesion force on fresh fractured interface was 32 nN (Figure 2h), which was approximately 25% higher than that on the surface region (Figure 2i). This observation suggested hydrogen bonds cut by fracture could self-reconstituted at the interface, making adhesion force be an indicator to reflect the state of hydrogen bonds. Therefore, due to the exchange of disulfide bonds and the recombination of hydrogen bonds, both non-crosslinked PTHF-4AD and the crosslinked PTHF-4AD-DAHP exhibited efficient self-healing performance at room temperature.

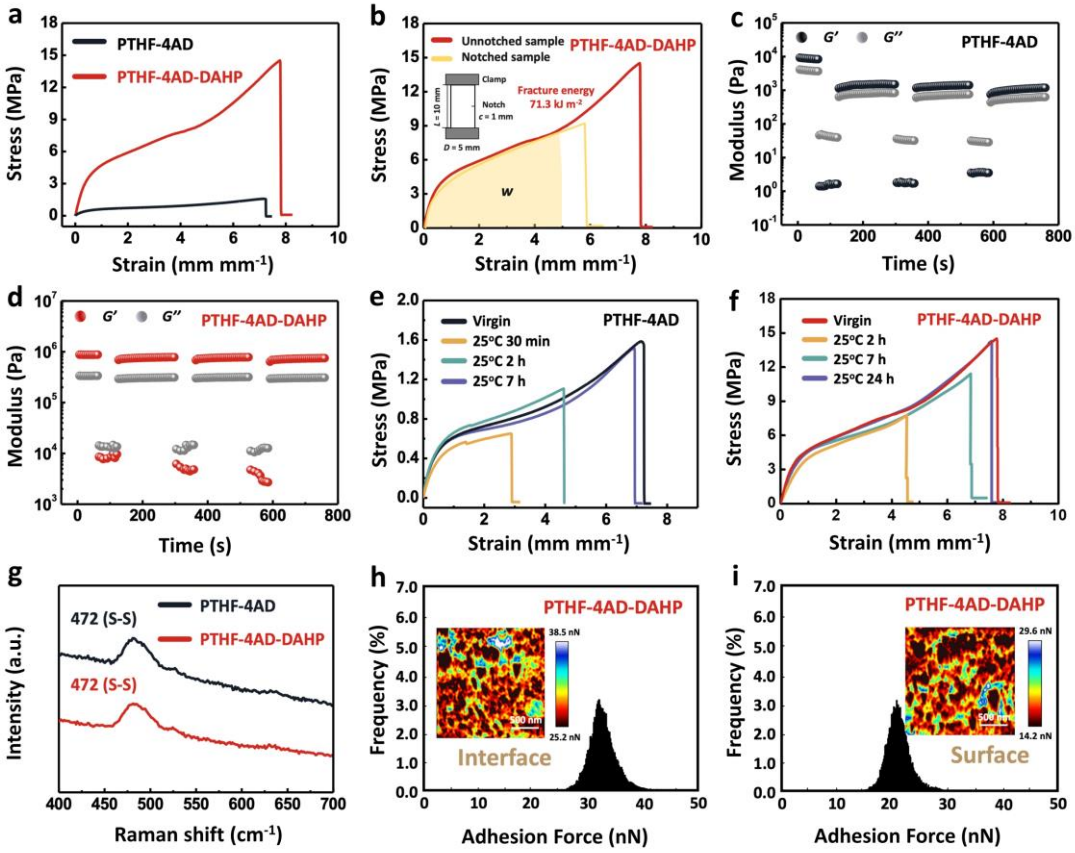

Figure 2. Mechanical and self-healing properties of PTHF-4AD and PTHF-4AD-DAHP. a) Tensile stress-strain curves of PTHF-4AD and PTHF-4AD-DAHP with a 500 N load cell at a stretching rate of 100 mm min^{-1}. b) Tensile stress-strain curves of PTHF-4AD-DAHP with and without notch (tensile rate 3 mm min^{-1}). Alternate step-strain measurements of c) PTHF-4AD and d) PTHF-4AD-DAHP at 25°C under a small strain of 1% and a large strain of 100% with

a fixed frequency at 10 rad s^{-1}. Tensile stress-strain curves of e) the self-healed PTHF-4AD and f) the self-healed PTHF-4AD-DAHP under different healing conditions. g) Raman spectra of PTHF-4AD and PTHF-4AD-DAHP in the range of 400-700 cm^{-1}. The distribution of adhesion force on h) the freshly fractured interface, and i) the surface region of PTHF-4AD-DAHP. Insets were the corresponding AFM mapping images (5×5 μm^2) for adhesion force measurements.

Then the ability to adhere PTHF-4AD to PTHF-4AD-DAHP was evaluated. A stripe of PTHF-4AD stained with rhodamine B and a strip of PTHF-4AD-DAHP stained with coumarin 6 were put into contact at one egde. After a contact at room temperature for 24 h, the strips healed together. The final integrated piece could undergo bending, spinning, and stretching deformation without connection failure or interface peeling (**Figure 3**a). Fluorescence microscopy images showed that the furrows between two stripes disappeared after 7 h, and then the surfaces started to interpenetrate to each other until complete connection after 24 h (Figure 3b). During the integrating process, urea and urethane groups allowed for rapid formation of multiple hydrogen bonds at the interface, while the presence of disulfide bonds imparted additional dynamical exchange at the interface, synergistically constructing the integrated material (Figure 3c). Additionally, the adhesive ability of PTHF-4AD to PTHF-4AD-DAHP was further tested with a 180-degree peeling test. The maximum peeling strength was 442 N/m, which was smaller than the real interfacial strength because of the cohesive failure (Figure S13, Supporting Information).

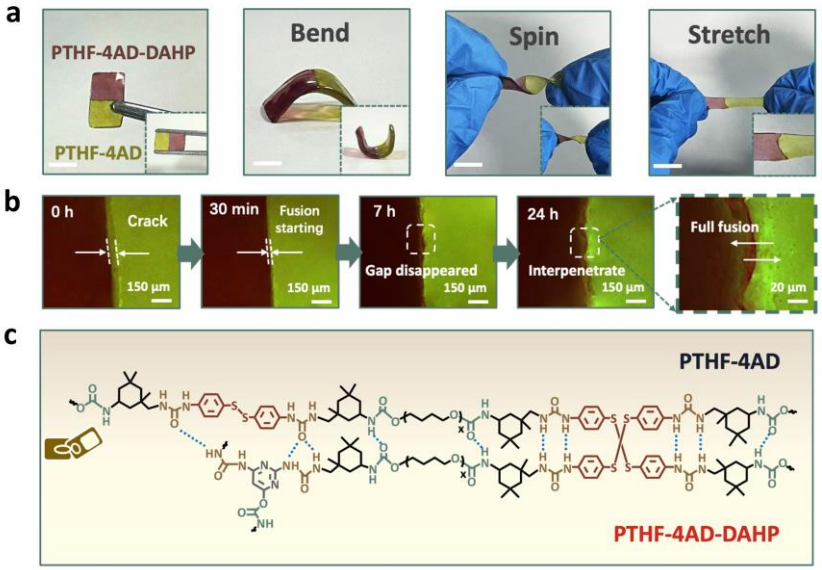

Figure 3. The fusion of PTHF-4AD and PTHF-4AD-DAHP. a) PTHF-4AD and PTHF-4AD-DAHP stripes fused to form a single piece that can undergo diverse deformations like bending,

spinning and stretching. Scale bar was 1 cm. b) Fluorescence microscopy images showing the inter-diffusion of rhodamine B-stained PTHF-4AD and coumarin 6-stained PTHF-4AD-DAHP under ambient conditions. c) Schematic representation of the reformation of hydrogen bonds and the exchange of disulfide bonds during the fusion.

2.3. Tensile deformation of PTHF-4AD-DAHP skeleton

The chemically crosslinked PTHF-4AD-DAHP was chosen as the material of the auxetic skeleton in this research. The relationship between morphology and mechanical property was first studied for a sample cut by laser into an auxetic skeleton with special topology structures that should exhibit negative Poisson's ratio in tensile mode. By virtue of FEA, the URES (unit displacement), von Mises (stress distribution), and ESTER (equivalent strain) of the skeleton structure with different parameters in the stretching process were first discussed to predict the shape morphing and mechanical behaviors of element units. Among complex auxetic structures, the re-entrant structure is a typical one where when the ribs are forced to move outward under a tensile load in horizontal direction, it expands along the vertical direction. Compared with the conventional re-entrant structure that had obvious stress concentration at the element junctions, the corrugated re-entrant structure could disperse well the stress (Figure S14, Supporting Information). Moreover, the "ABA" arrangement order of element units illustrated a more uniform equivalent stress distribution (Figure S15, Supporting Information).

With the corrugated re-entrant structure of the "ABA" arrangement order in hand, three geometric parameters for element units, including center angle α, chord length l, and beam width w, were synergistically considered, as the dimensions of element units were particularly important for the overall mechanical performance and auxetic effect. By setting the α of 90^{o} and the l of 5 mm, the corrugated re-entrant PTHF-4AD-DAHP-0.5, PTHF-4AD-DAHP-1.0, and PTHF-4AD-DAHP-1.5 were fabricated with the w of 0.5, 1.0, and 1.5 mm, respectively (Figure S16, Supporting Information). Tensile tests demonstrated that the fracture strength was 0.6, 3.2, and 4.0 MPa for PTHF-4AD-DAHP-0.5, PTHF-4AD-DAHP-1.0, and PTHF-4AD-DAHP-1.5, respectively, accompanied with the elongation at break of 509%, 400%, and 326% (**Figure 4**a), revealing the large reduction in mechanical performance compared with PTHF-4AD-DAHP elastomer without motif-cutting in Figure 2a. The variation trend of elongation at break was consistent with the simulation results in FEA, where the URES decreased with the rise of w from PTHF-4AD-DAHP-0.5 to PTHF-4AD-DAHP-1.5 (Figure 4b). During the full stretching process, their lateral strains were determined (Figure S17, Supporting Information), and the corresponding Poisson's ratio (v) can be deduced in Figure 4c, where the NPR effect

was observed over an extended strain window for these three skeletons. It is known that the good auxetic behavior is guaranteed by the high value of NPR that remains valid in a large strain range.[47] As such, PTHF-4AD-DAHP-1.0 was identified to have strong auxetic behavior as the minimum v = −0.42 and strain range of NPR = 0-143%, while PTHF-4AD-DAHP-0.5 (v_{min} = −0.18 and strain range of NPR= 0-145%) and PTHF-4AD-DAHP-1.5 (v_{min} = −0.38, strain range of NPR = 0-123%) showed relatively weak auxetic responses (Figure 4d). FEA results further confirmed that the stress concentration points reflected in von Mises of PTHF-4AD-DAHP-0.5 and PTHF-4AD-DAHP-1.5 were clearly observed, while were less visible in PTHF-4AD-DAHP-1.0 (Figure 4b), showing smooth and uniform distributed stress dispersion throughout the stretching process.

Figure 4e intuitively showed the Poisson's ratio (v) from the original state to the elongation of 50% in experiment and FEA. The value of v was −0.42, −0.38, −0.26, and −0.18 at a strain of 10%, 25%, 40%, and 50% in experiment, quite close to the v value of −0.46, −0.37, −0.28, and −0.22 under the same strain in FEA. Furthermore, the noise-free and smoother FEA data made it possible to forecast and predict auxetic behaviors. As shown in Figure 4f, the model-predicted trends and values resembled the experimental data, confirming the consistency from not only negative Poisson's ratio values but also strain range. Similar consistency between experiment and simulation was also observed for PTHF-4AD-DAHP-0.5 and PTHF-4AD-DAHP-1.5 by the evolution of Poisson's ratio plotted with the applied tensile strain (Figure S18, Supporting Information). Comprehensive considering the fracture strength, stress distribution, NPR effect, and elongation range of the NPR window, PTHF-4AD-DAHP-1.0 was considered as a suitable skeleton for preparing the integrated auxetic elastomer (IAE) in comparison with the other structured PTHF-4AD-DAHP.

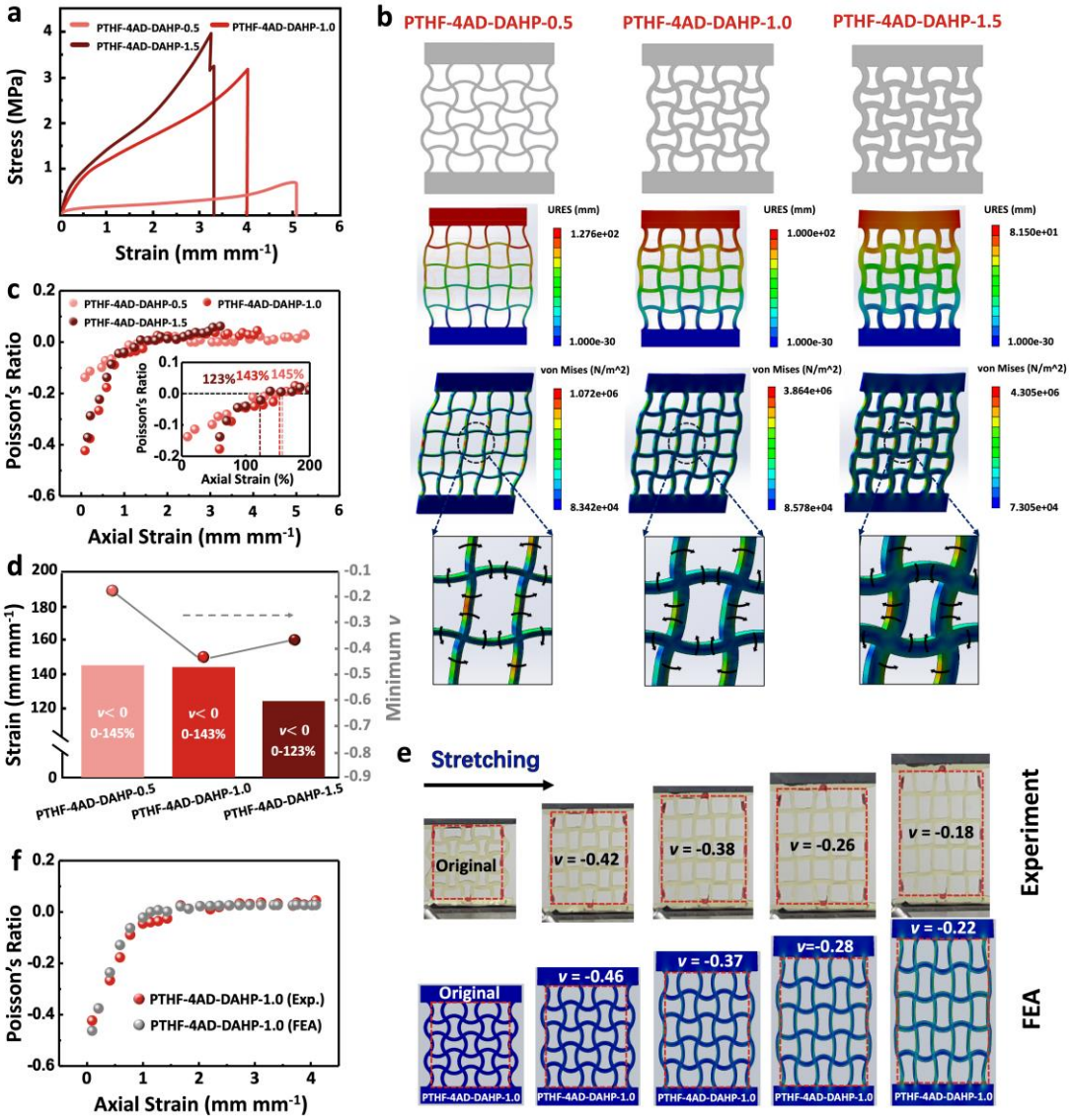

Figure 4. Tensile deformation of PTHF-4AD-DAHP skeleton. a) Tensile stress-strain curves of PTHF-4AD-DAHP-0.5, PTHF-4AD-DAHP-1.0, and PTHF-4AD-DAHP-1.5 with a 500 N load cell at a stretching rate of 100 mm min^{-1}. b) URES and von Mises of PTHF-4AD-DAHP-0.5, PTHF-4AD-DAHP-1.0, and PTHF-4AD-DAHP-1.5 under the tensile mode in FEA. c) Poisson's ratio of PTHF-4AD-DAHP-0.5, PTHF-4AD-DAHP-1.0, and PTHF-4AD-DAHP-1.5 as a function of axial strain, and d) the corresponding values of Poisson's ratio and occurrence strain range of NPR. e) Experimental and FEA screenshots of PTHF-4AD-DAHP-1.0 from the original state to elongation of 50%. The rectangle dashed lines marked the shape morphing area. f) Experimental and FEA Poisson's ratio of PTHF-4AD-DAHP-1.0 as a function of axial strain in the full stretch process.

2.4. Elaboration of integrated auxetic elastomers (IAE) and their mechanical properties

To remedy as far as possible the defect of mechanical behaviors of the PTHF-4AD-DAHP skeleton with corrugated re-entrant structure without losing its auxeticity, an unprecedented material preparation method was tried here. As depicted in Scheme 1b and Figure S19 (Supporting Information), PTHF-4AD-DAHP-1.0 skeleton, after being structured, was filled by the shape-complementary PTHF-4AD. By healing at 25ºC for 24 h under a pressure of 1 MPa, an integrated auxetic elastomer (IAE) with a skeleton-matrix structure was constructed. The resulting IAE was flat, void-free, and had no sharp soft-to-hard interface (**Figure 5**a), which revealed the complete healing. Tensile tests demonstrated that the incorporation of the PTHF-4AD matrix significantly improved the mechanical performance of IAE (Figure 5b). The IAE showed an extraordinary 5-fold increase in fracture strength (from 18 N of PTHF-4AD-DAHP-1.0 to 92 N of IAE) and a 1.5-fold increase in elongation at break (from 400% of PTHF-4AD-DAHP-1.0 to 600% of IAE) (Figure 5c). Note that this skeleton-matrix IAE showed an intriguing fracture behavior in the stretching process (Figure 5d). Firstly, it resisted most of the applied stress until the rupture took place at the edge of the skeleton under a high strain of 510% rather than fracturing globally (Stage 1). Upon further stretching to 525%, the stress was transferred to the soft PTHF-4AD matrix to dissipate more energy, reflecting a slight increase in stress from 80 to 84 N (Stage 2). Before the overall failure at the strain of 600%, other regions of IAE sequentially deformed and ruptured with notch extension (Stage 3). Apparently, the fracture of IAE occurred multiple times at different locations during the stretching process until the complete failure (Stage 4). In the whole stretching process, the energy was dissipative from small to large strains to enhance the toughness of IAE. Collectively, upon deformation of IAE, the interconnected hard skeleton not only effectively bore load but also preferentially ruptured to dissipate energy for avoiding stress concentration and resisting crack propagation, while the soft matrix played a cushioning role in fracture, helping dissipate energy and improving the overall mechanical properties of IAE. To further assess the elasticity and resilience of IAE, cyclic tensile tests were carried out. The gradient energy dissipation in cyclic stretching with increased strains and at different resting times under a strain of 200% verified the good reliability of IAE when undergoing repeated deformations. Moreover, the 50 successive cycles tests proved that the IAE possessed admirable fatigue resistance (Figure S20, Supporting Information).

The lateral strain of IAE was recorded during the stretching process (Figure S21, Supporting Information), and accordingly the Poisson's ratio was obtained (Figure 5e). The minimum v was −0.12 and the NPR effect appeared within a wide strain range of 0-104%, slight lower than

PTHF-4AD-DAHP-1.0. These experimental results were consistent with the simulation results from FEA (Figure 5f). In addition, the stress distribution at the former stage of the stretching process before the Poisson's ratio of zero was analyzed by FEA (inset, Figure 5f). Under the small strain, the stress distribution of IAE was uniform due to the initial restricted stress transfer. As the increase of strain, the skeleton dominated the stress distribution to resist deformation, while partial stress was shared by the matrix providing toughness to resist fracture.[48] As a result, the relatively uniform stress distribution of IAE avoided the danger of peeling caused by sharp stress concentration between hard skeleton and soft matrix, thus ensuring the deformation process and auxetic behavior of IAE. On the other hand, FEA simulation also confirmed the improvement of mechanical properties as shown in Figure 5g. Under the same applied force as the experiment, the displacement value of IAE decreased, according to the simulation, by an order of magnitude (see contour plot of URES) compared with PTHF-4AD-DAHP-1.0 (Figure 4b), due to the constraint of PTHF-4AD matrix. Meanwhile, PTHF-4AD underwent the extension deformation inside IAE (see ESTRN Contour Plots) while dispersing the stress of PTHF-4AD-DAHP skeleton (see Mises Stress Contour Plots). On the basis of all experimental and simulation results, it was concluded that the integrated low-modulus matrix dispersed the stress that was originally concentrated on the skeleton. Consequently, the fracture toughness of the final IAE was improved while maintaining the NPR effect of its skeleton.

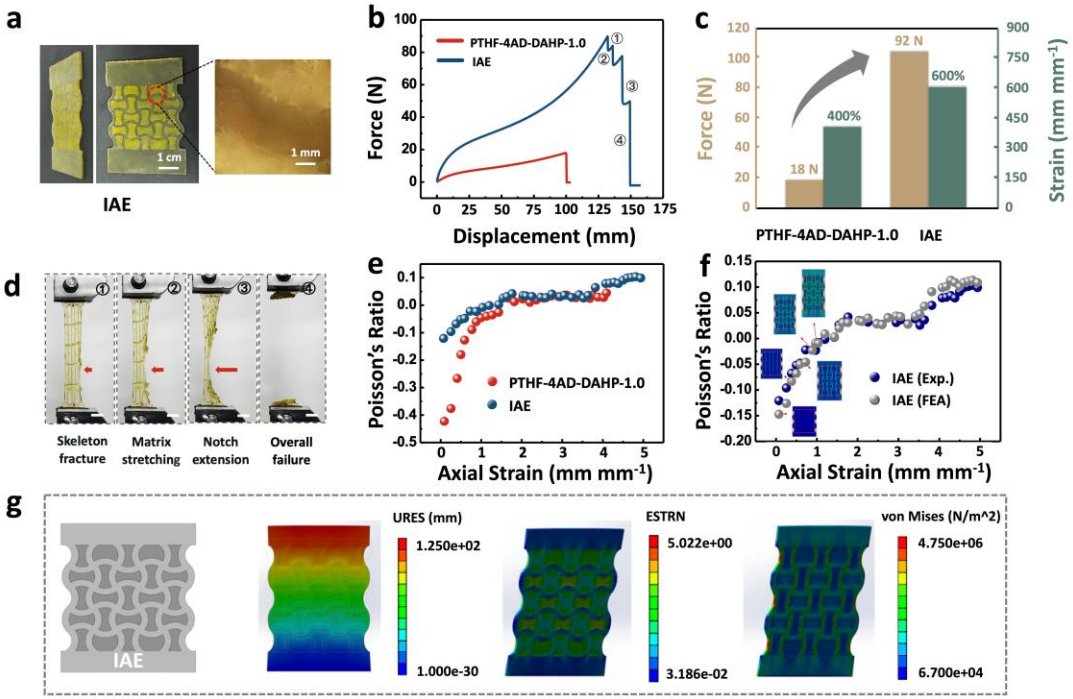

Figure 5. Integrated auxetic elastomers (IAE) with improved mechanical and auxetic properties. a) Photographs of IAE and its interface after healing. b) Tensile force-displacement curves of

PTHF-4AD-DAHP-1.0 and IAE, and c) the corresponding values of tensile force and elongation at break. d) Photographs of the stretching process of IAE showing fracturing behaviors including 4 stages. e) Poisson's ratio of PTHF-4AD-DAHP-1.0 and IAE as a function of axial strain. f) Experimental and FEA Poisson's ratio of IAE as a function of axial strain in the full stretch process. Inset were stress distribution images during stretching to 100% in FEA. g) URES, ESTRN, and von Mises of IAE under the condition of a stretching speed of 10 mm min^{-1} until the displacement of 125 mm. The color bar from red to blue indicated that the simulated value was from high to low, thus qualitatively showing the deformation behavior and stress and strain distribution.

3. Conclusion

In summary, we have synthesized a crosslinked poly(urethane-urea) (PTHF-4AD-DAHP) with high modulus and a non-crosslinked poly(urethane-urea) (PTHF-4AD) with low modulus. Due to their internal dynamic disulfide bonds and hydrogen bonds, both PTHF-4AD and PTHF-4AD-DAHP exhibited efficient self-healing performance at room temperature. Taking PTHF-4AD-DAHP as a corrugated re-entrant skeleton while PTHF-4AD as the shape-complementary filling matrix, a bio-inspired integrated auxetic elastomer (IAE) with skeleton-matrix structure was elaborated successfully through dual dynamic interfacial healing driven by disulfide bonds and hydrogen bonds. The resulting IAE was flat, void-free, and had no sharp soft-to-hard interface. Compared with the corrugated re-entrant skeleton, the IAE remedied the decline in mechanical performance caused by subtractive manufacturing while retaining its auxetic property. The fracture strength and elongation at the break of IAE were increased to 400% and 150% of the skeleton alone, while the IAE still reserved negative Poisson's ratio within a wide strain range of 0-104%. Both experimental and FEA simulation results revealed that the interconnected hard skeleton preferentially ruptured to dissipate energy for avoiding stress concentration and crack propagation, while the integrated low-modulus matrix dispersed the stress initially concentrated on skeleton. Consequently, the fracture toughness of the final IAE was improved while maintaining the NPR effect of its skeleton. This work solves the difficulties to fabricate comprehensive auxetic elastomers with robust mechanical properties and the NPR effect. The elaboration process of complementary shape-filling and dual dynamic interfacial healing paves a way for automatic scaled-up synthesis of modular heterogeneous materials, which could be a promising approach to manufacturing mechanically robust auxetic elastomers for the next generation of metamaterials. Certainly, due to the non-porous structure of IAE, its air permeability is weak compared with traditional auxetic structures with pores. This might

limit potential applications of IAE that require breathability, such as in the area of wound dressings and strain sensors. To solve this potential overcome, (1) the thickness of IAE can be reduced; (2) some functional components can be added to increase the breathability; (3) the direct contact area of IAE can be controlled when designing the devices.

4. Experimental Section

4.1 Synthesis of PTHF-4AD and PTHF-4ED. Initially, PTHF (16 g, 16 mmol) was charged into a flask and heated to 60°C, and then IPDI (7.47 g, 33.6 mmol) and DBTDL (32 μL, 0.054 mmol) were added and stirred for 3 h. After that, the chain extender 4-AD or 4-ED in DMAc was added, and the solution was stirred at 60°C for another 1 h. The resulting viscous solution was poured into a Teflon mold and then moved into a vacuum oven at 80°C for 36 h and 100°C for 12 h to remove the solvent. Lastly, the obtained product was transferred into a rectangular mold with a thickness of 1 mm and placed on a plate vulcanizer at 100°C for 3 h to afford the PTHF-4AD or PTHF-4ED elastomer.[45]

4.2 Synthesis of PTHF-4AD-DAHP and PTHF-4ED-DAHP. Initially, PTHF (15 g, 15 mmol) was added into a three-necked flask and heated to 60°C, and then IPDI (6.99 g, 31.5 mmol) and DBTDL (30 μL, 0.05 mmol) were added and stirred for 3 h. Afterward, the chain extender 4-AD or 4-ED and the crosslinker DAHP in DMSO were added into the solution and stirred at 60°C for another 1 h. The resulting viscous solution was poured into a Teflon mold and then moved into a vacuum oven at 100°C for 36 h and 120°C for another 12 h to remove the solvent. Finally, the obtained product was transferred into a rectangular mold with a thickness of 0.8 mm and placed on a plate vulcanizer at 120°C for 3 h to afford the PTHF-4AD-DAHP or PTHF-4ED-DAHP elastomer.[45]

4.3 Elaboration of the integrated auxetic elastomer (IAE). Initially, as shown in Figure S19 (Supporting Information), the PTHF-4AD-DAHP elastomer was cut to the expected shapes. After that, the same structure was applied to PTHF-4AD elastomer with a slightly higher height. By filling the shape-complementary structure of PTHF-4AD matrix into the skeleton of PTHF-4AD-DAHP, the final integrated auxetic elastomer (IAE) was obtained via the dual dynamic interfacial healing process under a pressure of 1 MPa for 24 h.

Statistical Analysis

All data were obtained from at least three independent samples and expressed as the mean ± standard deviation (n = 3 for polymer characterization; n = 5 for mechanical studies).

Supporting Information

Supporting Information is available from the Wiley Online Library or from the author.

Acknowledgements

This work is supported by the Open Fund of Anhui Province Key Laboratory of Environment-friendly Polymer Materials, and National Key Laboratory of Science and Technology on Advanced Composite (KZ42191814).

Conflict of Interest

The authors declare no conflict of interest.

Data Availability Statement

Research data are not shared.

Received: ((will be filled in by the editorial staff))
Revised: ((will be filled in by the editorial staff))
Published online: ((will be filled in by the editorial staff))

References

[1] A. Papadopoulou, J. Laucks, S. Tibbits, *Nat. Rev. Mater.* **2017**, 2,17078.

[2] J. I. Lipton, R. MacCurdy, Z. Manchester, L. Chin, D. Cellucci, D. Rus, *Science* **2018**, 360, 632.

[3] K. K. Dudek, J. A. I. Martinez, G. Ulliac, L. Hirsinger, L. Wang, V. Laude, M. Kadic, K. K. Dudek, *Adv. Mater.* **2023**, 35, 2210993.

[4] C. Song, B. Zou, Z. Cui, Z. Liang, J. Ju, *Adv. Funct. Mater.* **2021**, 31, 2101395.

[5] Y. Wang, X. Zhang, Z. Li, H. Gao, X. Li, *Proc. Natl. Acad. Sci. U. S. A.* **2022**, 119, e2119536119.

[6] N. Pagliocca, K. Z. Uddin, I. A. Anni, C. Shen, G. Youssef, B. Koohbor, *Mater. Des.* **2022**, 215, 110446.

[7] A. Farzaneh, N. Pawar, C. M. Portela, J. B. Hopkins, *Nat. Commun.* **2022**, 13, 1041.

[8] Y. Jiang, Z. Liu, N. Matsuhisa, D. Qi, W. R. Leow, H. Yang, J. Yu, G. Chen, Y. Liu, C. Wan,

Z. Liu, X. Chen, *Adv. Mater.* **2018**, 30, 1706589.

[9] P. Chansoria, J. Blackwell, E. L. Etter, E. E. Bonacquisti, N. Jasiewicz, T. Neal, S. A. Kamal, J. Hoque, S. Varghese, T. Egan, J. Nguyen, *Adv. Funct. Mater.* **2022**, 32, 2207590.

[10] J. Qi, Z. Chen, P. Jiang, W. Hu, Y. Wang, Z. Zhao, X. Cao, S. Zhang, R. Tao, Y. Li, D. Fang, *Adv. Sci.* **2022**, 9, 2102662.

[11] I. Apsite, A. Biswas, Y. Li, L. Ionov, *Adv. Funct. Mater.* **2020**, 30, 1908028.

[12] X. Zhou, L. Ren, Z. Song, G. Li, J. Zhang, B. Li, Q. Wu, W. Li, L. Ren, Q. Liu, *Composites, Part B* **2023**, 254, 110585.

[13] M. Wan, K. Yu, H. Sun, *Compos. Struct.* **2022**, 279, 114791.

[14] K. Sathish, S. S. Kumar, R. T. Magal, V. Selvaraj, V. Narasimharaj, R. Karthikeyan, G. Sabarinathan, M. Tiwari, A. E. Kassa, A. Parthiban, *Adv. Mater. Sci. Eng.* **2022**, 1, 6892641.

[15] S. R. Petersen, H. Prydderch, J. C. Worch, C. J. Stubbs, Z. Wang, J. Yu, M. C. Arno, A. V. Dobrynin, M. L. Becker, A. P. Dove, *Angew. Chem. Int. Ed.* **2022**, 61, e202115904.

[16] J. Kang, D. Son, G. N. Wang, Y. Liu, J. Lopez, Y. Kim, J. Y. Oh, T. Katsumata, J. Mun, Y. Lee, L. Jin, J. B. Tok, Z. Bao, *Adv. Mater.* **2018**, 30, 1706846.

[17] M. Burnworth, L. Tang, J. R. Kumpfer, A. J. Duncan, F. L. Beyer, G. L. Fiore, S. J. Rowan, C. Weder, *Nature* **2011**, 472, 334.

[18] E. Filippidi, T. R. Cristiani, C. D. Eisenbach, J. H. Waite, J. N. Israelachvili, B. K. Ahn, M. T. Valentine, *Science* **2017**, 358, 502.

[19] D. G. Mackanic, X. Yan, Q. Zhang, N. Matsuhisa, Z. Yu, Y. Jiang, T. Manika, J. Lopez, H. Yan, K. Liu, X. Chen, Y. Cui, Z. Bao, *Nat. Commun.* **2019**, 10, 5384.

[20] X. Ming, A. Wei, Y. Liu, L. Peng, P. Li, J. Wang, S. Liu, W. Fang, Z. Wang, H. Peng, J. Lin, H. Huang, Z. Han, S. Luo, M. Cao, B. Wang, Z. Liu, F. Guo, Z. Xu, C. Gao, *Adv. Mater.* **2022**, 34, 2201867.

[21] J. Zhou, X. Xu, Y. Xin, G. Lubineau, *Adv. Funct. Mater.* **2018**, 28, 1705591.

[22] X. Xue, D. Zhang, Y. Wu, R. Xing, H. Li, T. Yu, B. Bai, Y. Tao, M. D. Dickey, J. Yang, *Adv. Funct. Mater.* **2022**, 33, 2210553.

[23] Y. Wang, J. Li, L. Sun, H. Chen, F. Ye, Y. Zhao, L. Shang, *Adv. Mater.* **2023**, e2211731.

[24] Y. Fujisawa, A. Asano, Y. Itoh, T. Aida, *J. Am. Chem. Soc.* **2021**, 143, 15279.

[25] W. Xu, D. Ravichandran, S. Jambhulkar, Y. Zhu, K. Song, *Adv. Funct. Mater.* **2021**, 31, 2009311.

[26] G. Chen, X. Deng, L. Zhu, S. Handschuh-Wang, T. Gan, B. Wang, Q. Wu, H. Fang, N. Ren, X. Zhou, *J. Mater. Chem. A* **2021**, 9, 10953.

[27] N. S. Ha, G. Lu, *Composites, Part B* **2020**, 181, 107496.

[28] M. J. Allen, H. M. Lien, N. Prine, C. Burns, A. K. Rylski, X. Gu, L. M. Cox, F. Mangolini, B. D. Freeman, Z. A. Page, *Adv. Mater.* **2023**, 35, 2210208.

[29] S. Jiang, J. Liu, W. Xiong, Z. Yang, L. Yin, K. Li, Y. Huang, *Adv. Mater.* **2022**, 34, 2204091.

[30] F. Barthelat, Z. Yin, M. J. Buehler, *Nat. Rev. Mater.* **2016**, 1, 16007.

[31] B. S. Lazarus, A. Velasco-Hogan, T. Gómez-del Río, M. A. Meyers, I. Jasiuk, *J. Mater. Res. Technol.* **2020**, 9, 15705.

[32] X. Zhou, B. Guo, L. Zhang, G. H. Hu, *Chem. Soc. Rev.* **2017**, 46, 6301.

[33] Y. Zhu, Q. Shen, L. Wei, X. Fu, C. Huang, Y. Zhu, L. Zhao, G. Huang, J. Wu, *ACS Appl. Mater. Interfaces* **2019**, 11, 29373.

[34] N. D. Dolinski, Z. A. Page, E. B. Callaway, F. Eisenreich, R. V. Garcia, R. Chavez, D. P. Bothman, S. Hecht, F. W. Zok, C. J. Hawker, *Adv. Mater.* **2018**, 30, 1800364.

[35] W. Zhao, Z. Zhang, J. Hu, X. Feng, J. Xu, Y. Wu, S. Yan, *Chem. Eng. J.* **2022**, 446, 137305.

[36] J. Xu, P. Chen, J. Wu, P. Hu, Y. Fu, W. Jiang, J. Fu, *Chem. Mater.* **2019**, 31, 7951.

[37] Z. Zhang, N. Ghezawi, B. Li, S. Ge, S. Zhao, T. Saito, D. Hun, P. F. Cao, *Adv. Funct. Mater.* **2020**, 31, 2006298.

[38] S. M. Kim, H. Jeon, S. H. Shin, S. A. Park, J. Jegal, S. Y. Hwang, D. X. Oh, J. Park, *Adv. Mater.* **2018**, 30, 1705145.

[39] Y. Huang, H. Wu, Q. Wu, R. Li, J. Wu, *J. Mater. Chem. A* **2022**, 10, 24290.

[40] Y. Huang, W. Li, Y. Yang, Q. Wu, J. Wu, *Compos. Sci. Technol.* **2023**, 232, 109867.

[41] Y. Lai, X. Kuang, P. Zhu, M. Huang, X. Dong, D. Wang, *Adv. Mater.* **2018**, 30, 1802556.

[42] S. Ma, D. Webster, *Macromolecules* **2015**, 48, 7127.

[43] X. Xu, S. Ma, S. Wang, J. Feng, J. Zhu, *J. Mater. Chem. A* **2020**, 8, 11261.

[44] R. Guo, Q. Zhang, Y. Wu, H. Chen, Y. Liu, J. Wang, X. Duan, Q. Chen, Z. Ge, Y. Zhang, *Adv. Mater.* **2023**, 2212130.

[45] Y. Cai, L. Yan, Y. Wang, Y. Ge, M. Liang, Y. Chen, H. Zou, S. Zhou, *Chem. Eng. J.* **2022**, 436, 135156.

[46] H. Gong, J. Wu, Z. Zhao, Z. Guo, L. Gao, B. Zhang, M.-H. Li, J. Hu, *Chem. Eng. J.* **2022**, 446, 137392.

[47] K. Wang, Y.-H. Chang, Y. Chen, C. Zhang, B. Wang, *Mater. Des.* **2015**, 67, 159.

[48] E. Ducrot, Y. Chen, M. Bulters, R. P. Sijbesma, C. Creton, *Science* **2014**, 344, 186.